Ocean Engineering 74 (2013) 61–71

Contents lists available at ScienceDirect

Ocean Engineering

journal homepage: www.elsevier.com/locate/oceaneng

Nearshore wave field simulation at the lee of a large island

Sotiria Anastasiou, Georgios Sylaios *

Laboratory of Ecological Engineering & Technology, Department of Environmental Engineering, Democritus University of Thrace, 67100 Xanthi, Greece

ARTICLE INFO

Article history:
Received 11 February 2013
Accepted 21 September 2013

Keywords:
SWAN model
ELCOM model
Model validation
Return period
North Aegean Sea

ABSTRACT

The ability of SWAN model to adequately reproduce the complex wave field at the lee of a large island (Thassos Island, North Aegean Sea) is examined herein. SWAN model was forced by the POSEIDON wind and wave offshore buoy and applied on three-nested grids under stationary mode, in direct coupling to a three-dimensional hydrodynamic model. SWAN model results were validated against in-situ observations at the sheltered nearshore zone, exhibiting fair underestimations in the computation of wave parameters, especially for waves entering the low-resolution computational grid. Cross-correlation analysis on the concurrent dataset revealed that northward propagating waves reach the nearshore zone in 4–5 h, while a time-lag of nearly 12 h was shown for the southward propagating waves. SWAN results at the nearshore field indicated a significant wave energy reduction at the sheltered region (~47%), associated with significant wave directional change. The coupling of SWAN to ELCOM improved model's performance on computing the wave propagation direction. The validated model was run under extreme wind and wave conditions illustrating that Athos Peninsula diffracts the southern waves, reducing their energy as they propagate around Thassos Island, thus inducing an asymmetry in favor of south-eastern waves.

1. Introduction

As waves propagate from the open sea towards the coast, wave field transformation occurs, enhancing complicated physical processes such as the combination of refraction–diffraction, the non-linear energy redistribution between wave quadruplets and wave triads and the energy dissipation processes, like the depth-induced wave breaking, the wave energy decay by bottom friction and the wave back-scattering (Alari et al., 2008). Moreover, the wave field appears highly complex in nearshore areas at the lee of islands and headlands, as the sheltering effect is induced, providing significant repercussions to the large-scale wave trains arriving in the area from the open sea (Rusu et al., 2008; Breivik et al., 2009). Sheltering has the following effects on the wave field at downwind locations: (a) the wave heights are significantly reduced, compared to unsheltered areas, and this variability increases as wave heights increase; (b) the mean wave direction turns towards the island especially under wind-generation conditions; and (c) the mean wave period is reduced since part of the wave field is generated under fetch limited conditions (Niclasen and Simonsen, 2005).

Wave transformation due to refraction and diffraction at the lee area of a large island can also be modeled through analytical solutions of the Helmholtz equation and the linear shallow-water equation, provided that the area has simple bottom geometry (e.g., cylindrical, conical or circular island) and particular wave type (long or short wave). These deficiencies were improved by the introduction of the mild-slope equation, becoming the appropriate method to describe the combined wave refraction–diffraction processes on slowly varying water depths. However, the absence of field data for the problem of combined wave refraction and diffraction around an island and the lack of analytical solutions to the original mild-slope equation for general wave conditions, led to the verification of the available analytical solutions with results from numerical models (Liu et al., 2004). Third generation spectral numerical models, like SWAN, appear able to reproduce adequately the wave field in areas with irregular bathymetry, considering the complex physical processes as the combined refraction–diffraction and the triad wave–wave interactions induced by the presence of large islands (Rusu et al., 2008). SWAN model has been widely popular in applications for wave climate description and/or wave hindcasting in open to ocean nearshore zones (Cuchiara et al., 2009; Lee et al., 2010; Dragani et al., 2010), elongated bays and seas (Alari et al., 2008; Caliskan and Valle-Levinson, 2008; Dykes at al., 2009), or even along coastlines sheltered by small islands (Browne et al., 2007; Breivik et al., 2009; Herman et al., 2009).

The purpose of the present work is the application and validation of a nested-grid SWAN numerical model, aiming to describe the wave characteristics at the lee area of a large, almost

* Corresponding author. Tel./fax: +30 25410 79398.
E-mail address: gsylaios@env.duth.gr (G. Sylaios).

0029-8018/$ - see front matter © 2013 Elsevier Ltd. All rights reserved.
http://dx.doi.org/10.1016/j.oceaneng.2013.09.013

circular island, in combination to the influence of strong along-channel currents. Keramoti coastline, located northwards of Thassos Island (Thracian Sea), where strong alongshore flow exists (Sylaios et al., 2013), was selected as an appropriate area for this testing. At the nearshore, fine resolution grid, SWAN model was tightly coupled to a three-dimensional circulation model (ELCOM, Estuary, Lake and Coastal Ocean Model), developed by the Centre for Water Research at the University of Western Australia (Hodges and Dallimore, 2001). Model results obtained from the stationary SWAN mode, for the lower level of spatial resolution grid, under real-time wind and offshore wave conditions were compared to nearshore wave data, recorded in the lee side of Thassos Island. After validation, the model was run under the 25, 50 and 100-year return values for offshore waves and winds, aiming to simulate the response of the sheltered area on extreme events.

2. Models description and setup

2.1. SWAN model description

SWAN is a third-generation phase-averaged spectral model, based on the following wave action balancing equations, capable of simulating wave evolution, frequency downshift, shoaling and refraction in the deep and nearshore water (Booij et al., 1999):

$$\frac{\partial N}{\partial t}+\frac{\partial}{\partial x}(U+c_x)N+\frac{\partial}{\partial y}(V+c_y)N+\frac{\partial}{\partial \sigma}c_\sigma N+\frac{\partial}{\partial \theta}c_\theta N=\frac{S_{tot}}{\sigma} \quad (1)$$

with

$$S_{tot}=S_{in}+S_{wc}+S_{nl4}+S_{bot}+S_{brk}+S_{nl3} \quad (2)$$

where N is the wave action spectral density function; σ and θ are the angular frequency and the direction of a component wave; c_x and c_y are the group velocities in the x and y directions, respectively; c_σ and c_θ are the characteristic velocities in the σ and θ directions, respectively; S_{tot} is the source term, and U and V are the current velocities in the x and y directions, respectively. The first term expresses the local variation rate of action density in time, the second and third terms express the propagation of wave energy in the two-dimensional Cartesian geographic space, while the fourth and fifth terms represent the depth-induced and current-induced wave refraction. The right-hand side represents processes that generate, dissipate or redistribute wave energy. In deep water, three source terms are employed. These are the transfer of energy from the wind to the waves, S_{in}, the dissipation of wave energy due to whitecapping, S_{wc}, and the nonlinear transfer of wave energy due to quadruplet (four-wave) interaction, S_{nl4}. In shallow water, dissipation due to bottom friction, S_{bot}, depth-induced breaking, S_{brk}, and nonlinear triad (three-wave) interaction, S_{nl3}, are additionally accounted for.

2.2. SWAN model set-up

The SWAN wave model (version 40.72) was implemented with the nominal formulations of the physical processes, to describe the wave characteristics at the lee of Thassos Island. This SWAN version incorporates the diffraction impact on wave propagation only in Cartesian co-ordinates, in a not fully tested phase decoupled mode (Rusu et al., 2008). The model was run using the Komen et al. (1994) wind input parameterizations and the default JONSWAP bottom friction considerations. The wave growth term of Cavaleri and Malanotte-Rizzoli (1981) was used and the source terms included white-capping dissipation, four-wave non-linear interactions, bottom friction, depth-induced breaking, and triad wave–wave interactions. The model was run in a stationary mode, meaning that $\partial N/\partial t=0$ in Eq. (1), assuming that waves propagate instantaneously through the model domain. In this mode, time is removed as a model variable, but the integration in the geographical space is still carried out iteratively, representing a three hours time step.

In order to achieve the required spatial downscaling for the produced wave field, three rectangular bilinear grids of increasingly higher resolution were used. The coarse grid covers the entire study area (North Aegean Sea), the second medium nested grid covers the Western Thracian Sea, including the Islands of Thassos and Thassopoula, and the third fine resolution grid extends from the Nestos River mouth until the coastline of Keramoti (Fig. 1). The geometric and geographical characteristics for each grid of the above described triple nesting are shown in Table 1.

SWAN model was implemented by two different configurations: in the first, all islands were considered in the computational grid as ‘land’, thus absorbing all incoming wave energy, while in the second case islands were considered as ‘obstacles’ in the propagation of the wave field, having zero wave transmission and reflection coefficients. This second choice was found more appropriate since the required proportions between wavelength and grid cell size for all three nestings failed to fulfill the prerequisite for direct diffraction calculation. Therefore, diffraction in the wave field was indirectly computed through obstacle's influence obtaining adequate results.

2.3. SWAN input and validation datasets

Initially, SWAN model was run to simulate the wave field for the time period between 8 December 2007 03:40 and 17 February 2008 09:40, with a time increment of three hours producing a total number of 74 cases. During this period, wave boundary conditions for the coarse resolution grid were obtained from the POSEIDON offshore wave buoy located near Athos Peninsula (39.96°N, 24.72°E, water depth 220 m) (Fig. 1). Analytical description of the POSEIDON sea observatory network operating by the Institute of Oceanography of the Hellenic Centre for Marine Research (HCMR) is presented by Soukissian et al. (1999, 2002). The most important recorded wave parameters are the spectral significant wave height H_{m0}, the mean zero-up-crossing T_{02}, and the mean wave direction θ_W (Soukissian et al., 2002). The wind fields for all SWAN model simulations were acquired from the NOAA Air Resources Laboratory (http://www.arl.noaa.gov/ready/amet.html), produced by the Global Data Assimilation System (GDAS), to derive wind data with 3-h interval at 12, 9 and 4 grid points, for the coarse, medium and high resolution grids, respectively.

SWAN model results at the nearshore area (fine resolution grid) were validated against the wave characteristics recorded by an upward-facing bottom-mounted Acoustic Doppler Current Profiler (ADCP, TRDI Sentinel 300 kHz), deployed at the coastal zone of Keramoti (40°51′284″N, 24°38′659″E, 23 m depth) (Fig. 1). The deployment point of the nearshore ADCP station was selected to induce the maximum island sheltering effect. The system is equipped with a Wave Array for directional wave measurements, a directional current meter, a tide gauge, a water temperature and a turbidity sensor. Directional wave data were sampled for 20 min every 3 h at a sampling rate of 2 Hz giving a maximum frequency of 1 Hz for wave characteristics. The system measures wave parameters such as significant wave height H_S (in m), peak period T_P (in s), direction of wave propagation in relation to the north (in degrees), and sea level variation (in m). The system was deployed during the period 20 July 2007–18 May 2008 producing a total of 2,422 datasets. Cubic spline interpolation routines were utilized to derive the ADCP recorded missing values (2.7% of the whole

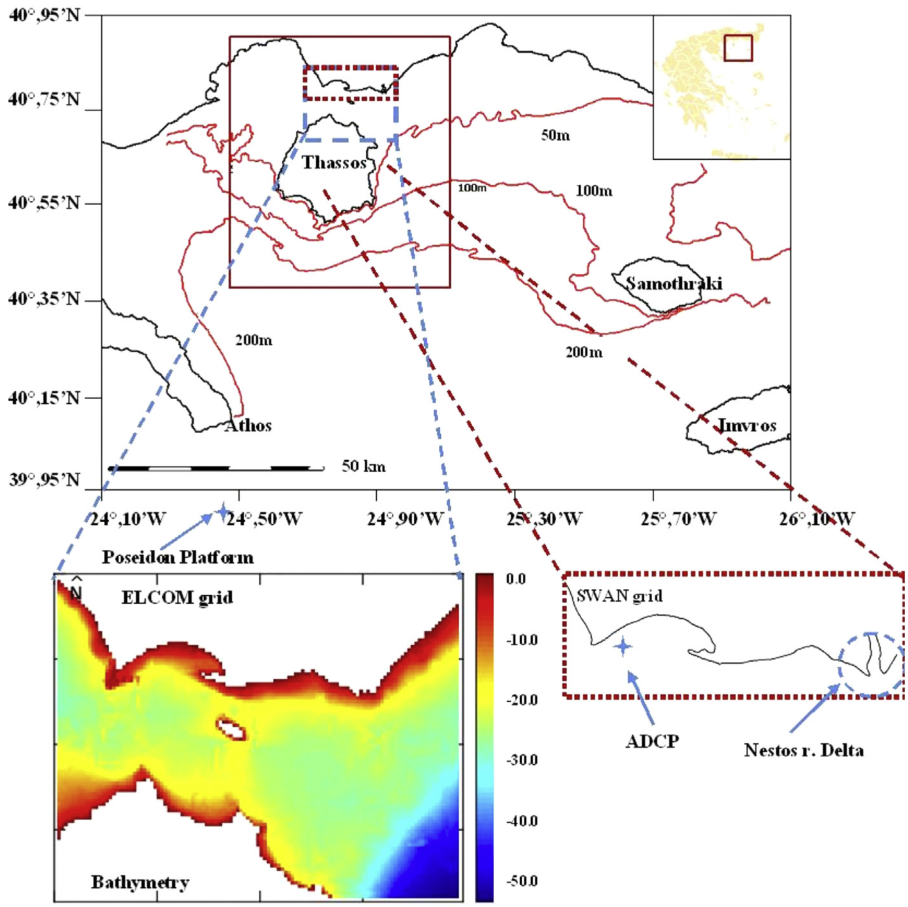

Fig. 1. Map of the study area (North Aegean Sea), indicating coverage of the three computational grids and location of the wave recording stations.

Table 1
Computational grids for SWAN simulations.

Grid description	Dimensions (Easting × Northing)	Cell grid size ($dx=dy$)	Geographic co-ordinates	Boundary conditions imposed
Coarse resolution grid	164 km × 112 km	1000 m	39°95′N, 24°10′E – SW point 41° 05′N, 25° 95′E – NE point	Significant wave height, period and direction from POSEIDON buoy; wind data at all grid points from NOAA meteorological model.
Medium resolution grid	54.9 km × 47.4 km	300 m	40° 35′N, 24° 30′E – SW point 40° 95′N, 24° 90′E – NE point	Model output from the coarse resolution grid along all open boundaries; wind data at all grid points from NOAA meteorological model.
Fine resolution grid	16.35 km × 5.30 km	50 m	40°84′N, 24°60′E – SW point 40°88′N, 24°80′E – NE point	Model output from the medium resolution grid along all open boundaries; wind data at all grid points from NOAA meteorological model.

dataset), after testing the accuracy of various interpolation techniques (linear, polynomial and nearest neighbor).

All model runs involved the demarcation of waves into: (a) the waves entering the computational grid (northerly propagating waves), and (b) the waves exiting the computational grid (southerly propagating waves), based on the measurements obtained at POSEIDON station. To compare wave directions at the ADCP site, wave propagation angles were transformed as (Sylaios et al., 2009)

$$\Phi=\left\{\begin{array}{l}1-(\Psi/180)\ \text{if}\ 0^\circ\le\Psi\le180^\circ\\ (\Psi-180)/180\ \text{if}\ 180^\circ\le\Psi\le360^\circ\end{array}\right\}\tag{3}$$

where Ψ is the wave propagation direction and Φ is the transformed direction varying within [0, 1].

2.4. SWAN validation criteria

SWAN model results were compared to in-situ observations at ADCP deployment and model's performance was assessed using the following criteria:

(a) the determination coefficient, R^2, defined as

$$R^2=\frac{ssr}{sst}\tag{4}$$

where $ssr=\sum_{i=1}^{N}(\widehat{y}_i-\overline{y})^2$ and $sst=\sum_{i=1}^{N}(y_i-\overline{y})^2$ with y_i the observed time-series, $\widehat{y}_i$ the corresponding modeled values, $\overline{y}$ the mean observed value, and N the total number of dataset. The closer R^2 is to 1.0 the less the points are scattered around the straight regression line.

(b) the root mean squared error (RMSE) and the scattered index (SI) of the modeled and observed values, defined as

$$RMSE = \sqrt{\frac{\sum_{i=1}^{N}(y_i - \hat{y}_i)^2}{N}} \quad (5)$$

$$SI = \frac{RMSE}{\bar{y}} \times 100 \quad (6)$$

The parameters *RMSE* and *SI* have to be as close to 0.0 as possible for good model performance.

(c) The Index of Agreement (IA), defined as (Willmott et al., 1985)

$$IA = 1 - \frac{\sum_{i=1}^{N}|\hat{y}_i - y_i|}{\sum_{i=1}^{N}(|\hat{y}_i - \bar{y}| + |y_i - \bar{y}|)} \quad (7)$$

The parameter of *IA* has to be as close to 1.0 as possible.

(d) The mean absolute error (MAE), defined as

$$MAE = \frac{1}{N}\sum_{i=1}^{n}|\hat{y}_i - y_i| \quad (8)$$

(e) The relative error (RE), defined as

$$RE = \sum_{i=1}^{n}\frac{y_i - \hat{y}_i}{y_i} \quad (9)$$

2.5. ELCOM model description and coupling setup

ELCOM is a three-dimensional circulation model that provides the wind-, tidal- and density-flow field in the studied area. The model solves the RANS equations (Reynolds-Averaged Navier–Stokes), using both hydrostatic and Boussinesq approximations. A semi-implicit numerical scheme is adopted applied on a finite-volume framework using rectangular Cartesian cells (Arakawa-C grid stencil) (Hodges et al., 2000). Horizontal grid spacing is fixed, whereas the vertical spacing may vary as a function of depth, but it is always horizontally uniform. The adapted TRIM approach for scalar conservation and elimination of numerical diffusion (Casulli and Cheng, 1992), and the implementation of a mixed-layer turbulence closure scheme is followed (Hodges et al., 2000).

Present model configuration at the nearshore grid involved 96×119 cells of 200 m horizontal resolution and 16 vertical layers with gradually increasing thickness. This configuration provided the instantaneous three-dimensional velocity field at four adjacent SWAN grid cells ($\Delta x = \Delta y = 50$ m). Caution was given on the discretization of the surface and bottom model cells at the same level as the ADCP bins. Open-sea boundary conditions were provided by a North Aegean Sea high resolution model (Kokkos and Sylaios, 2012). Meteorologic data, river flows and scalar values at boundaries were similar to those described by Kamidis et al. (2011).

The SWAN and ELCOM models were integrated and coupled in a manner that information may be exchanged between them without time-consuming interpolations. An interface in Matlab was developed for that reason, and the coupling interval was taken equal to the SWAN time step. On each coupling interval, ELCOM was run first, since nearshore wave properties could be dependent on circulation. The water currents produced by ELCOM on each time-step were imported in SWAN to force its solution on the next time-step. Such scheme was developed for the first time, as previous efforts involved the coupling of SWAN and ADCIRC models (Dietrich et al., 2011, 2012).

2.6. Return period values for offshore winds and waves

The Peaks-Over-Threshold (POT) technique was followed to estimate the return period values for offshore wind speeds and significant wave heights, utilizing the POSEIDON dataset for the 2000–2010 period. The dataset consists of 14,128 wind and 10,459 wave values. In our analysis only the independent non-overlapping storms, with at least 6 h duration, exceeding a certain threshold (u) and separated by a minimum distance of 48 h between consecutive data points, were selected (Simiu and Heckert, 1996). Data were carefully checked for outliers to diminish extreme values produced by buoy measurement errors.

Threshold selection involved balancing between bias and variance, since the selection of a low threshold increases the number of exceedances, thus increasing the precision of the estimation, but this estimation becomes biased by some observations at the center of the distribution. A careful visual inspection of the *Q*–*Q* graph, Hill-plot and sample mean excess against thresholds plot leads to a subjective threshold determination method. In this latter plot, threshold may be determined as the higher level in which sample mean excesses are consistent with a straight line (Coles, 2001).

Assuming that the wind and wave values extracted following the above method were independent (representing maxima from different storms) and identically distributed (iid), the generalized extreme value (GEV) distribution can be applied to the extremes, as

$$F(x;\mu,\sigma,\xi) = \begin{cases} \exp[-(1+\xi((x-\mu)/\sigma))^{-1/\xi}], & \xi \neq 0, \\ \exp[-\exp(-((x-\mu)/\sigma))], & \xi = 0 \end{cases} \quad (10)$$

where $1+\xi(x-\mu)/\sigma > 0$, μ is a location parameter, σ is a scale parameter and ξ is the shape parameter which determines the nature of the tail of the distribution. These parameters are independent of the selected threshold. The cases $\xi > 0$, $\xi = 0$ and $\xi < 0$ correspond to the Fréchet, Gumbel and the reverse Weibull distributions, respectively. In case that selected storms belong to the Fréchet domain, their tails appear heavy and unbounded, implying that their domain of attraction for maxima is weighted towards extreme events. In the Gumbel domain, their tails decrease exponentially, while in the Weibull domain, their tails are bounded and an upper limit determined by $\mu - \sigma/\xi$.

In order to obtain return levels, the exceedance rates of thresholds u specified as $\lambda = P(X > u)$, are given by

$$\lambda = 1 - \exp\left\{-\frac{1}{N}\left[1+\xi\left(\frac{u-\mu}{\sigma}\right)\right]^{-1/\xi}\right\} \quad (11)$$

and the p-year return level z_p is obtained as

$$\hat{z}_p = u + \frac{\sigma^*}{\xi^*}[(\lambda p)^{\xi^*} - 1] \quad (12)$$

where $\xi^* = \xi$ and $\sigma^* = \sigma + \xi(u-\mu)$.

For both datasets, the estimation of GEV model parameters was performed following the Maximum Likelihood Estimator. Analysis was performed using the package extRemes in the R open source statistical software and by EVIM (Gençay et al., 2001) in Matlab.

3. Results

3.1. Offshore and nearshore wind and wave fields

Overall, 2422 concurrent measurements of wind and wave data obtained at the offshore POSEIDON platform and at the nearshore ADCP station were analyzed. Wind (speed and direction) obtained through NOAA/GDAS and wave (significant wave height, wave period and propagation direction) were recorded with a 3-h time-interval. The wind roses at both stations are shown in Fig. 2. At the offshore site, north-east winds (33.8%) dominate the area with generally higher wind speeds (mean: 6.9 m/s, max: 21 m/s). South (15.5%) and south-west (10.8%) winds play a secondary role in the

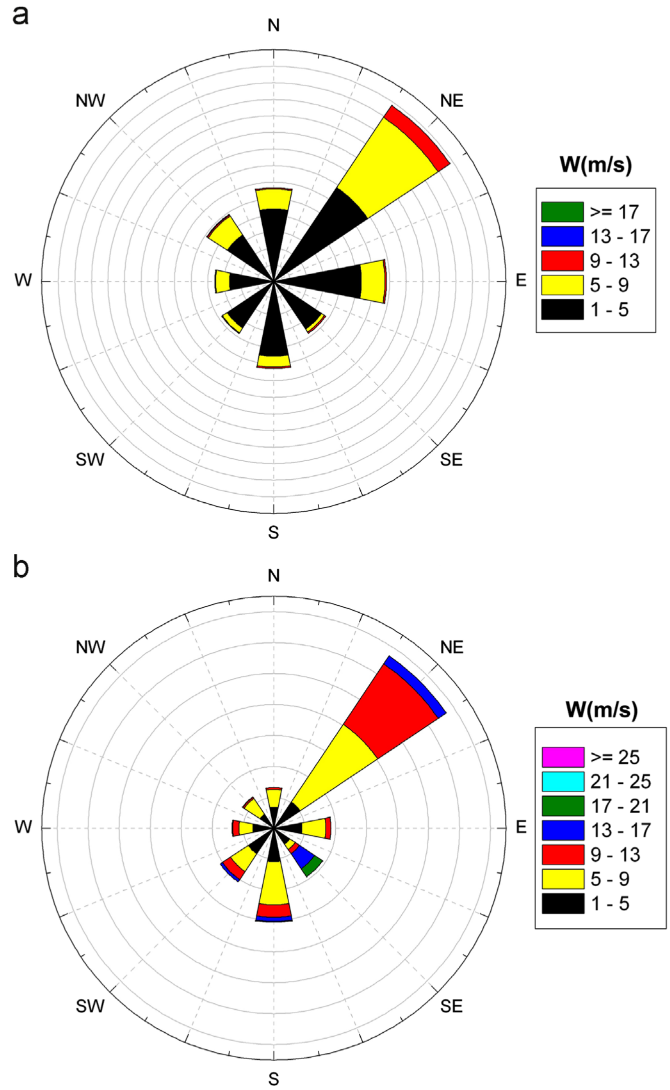

Fig. 2. Wind roses for: (a) the nearshore ADCP site; and (b) the offshore POSEIDON platform, recorded within the period 20 July 2007–18 May 2008.

meteorological regime at the offshore site. At the neashore field, the north-east direction dominance appears reduced (26.5%), with lower wind speeds (mean: 3.7 m/s, max: 15.8 m/s). Eastern (14.6%) and northern winds (12.1%) exhibit a lower occurrence level in the area.

Wave analysis illustrates that at the nearshore site, waves with significant wave heights ($H_S > 0.3$ m) occur at 60% of cases, while at the offshore site this occurrence represents waves of $H_S > 1$ m. Maximum H_S-values of 3.52 m and 1.51 m were recorded at the offshore and nearshore site, respectively (Table 2). Wave periods of these extreme events reached 10.0 s and 11.6 s, respectively. At the POSEIDON site, the higher wave heights ($H_S > 1.5$ m) propagate from north-east (44.4%) and south-west (26%) directions, while the most frequent waves occur from the north-east direction (35.3%, for all wave classes). Waves with H_S-value higher than 2 m are monitored mostly in the November–February period, exhibiting a relative frequency of 8%. At the sheltered nearshore ADCP station, waves mostly occur from the south-east (51.7%) and east (16.1%) directions (Fig. 3), with higher waves (> 0.8 m) being recorded between October and March from south-east (77.8%) and south-west (22.2%). The increased fetch of these directions plays the dominant role in the growth of these waves.

Table 2
Wave statistics for the offshore (POSEIDON Athos) and nearshore (ADCP) sites.

	POSEIDON Athos	ADCP
Significant wave height (H_S)		
Mean (m)	0.84	0.31
Standard deviation (m)	0.67	0.14
Minimum value (m)	0.00	0.13
Maximum value (m)	3.52	1.51
Variance (m)	0.46	0.02
Wave period (s)		
Mean (m)	4.66	3.85
Standard deviation (m)	1.42	1.00
Minimum value (m)	0.00	2.90
Maximum value (m)	10.00	11.60
Variance (m)	2.03	1.01

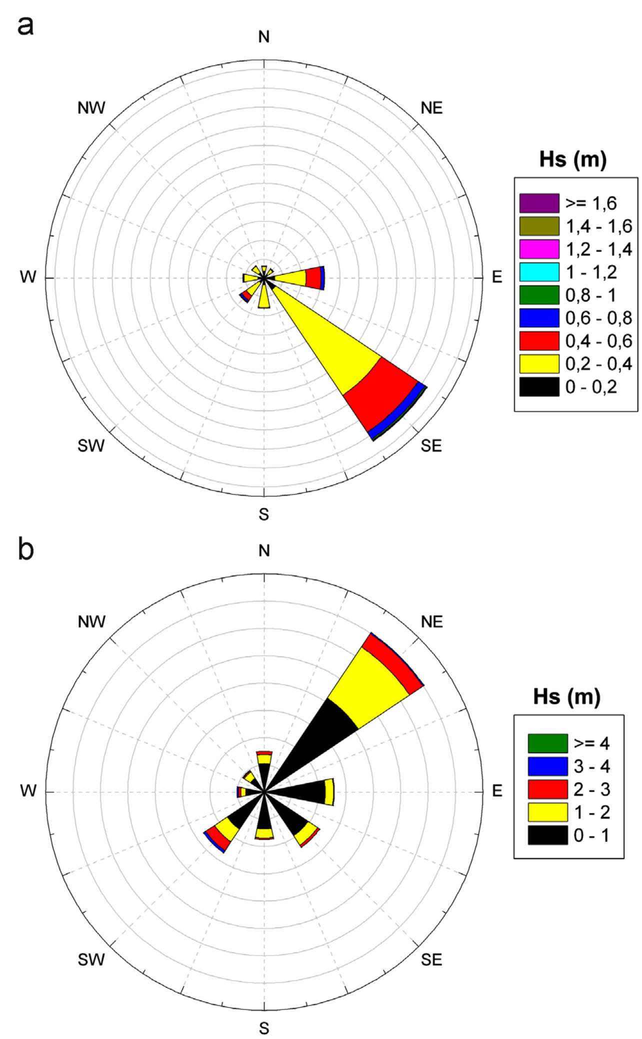

Fig. 3. Wave roses for: (a) the nearshore ADCP site; and (b) the offshore POSEIDON platform, recorded within the period 20 July 2007–18 May 2008.

3.2. *Offshore–nearshore waves interaction*

Waves recorded at POSEIDON were demarcated into: (a) waves entering the computational grid, thus propagating northwards, and (b) waves exiting the computational grid, thus southerly propagating waves. Cross-correlation analysis between the waves recorded at the POSEIDON platform and those measured at the ADCP deployment are shown in Fig. 4.

It occurs that for the northwards propagating waves, a lag of 2 time-intervals exists in the significant wave height series (Fig. 4a). This seems consistent with theoretical considerations, as the waves with the mean wave period in POSEIDON ($T\sim$4–5 s), propagate at a phase speed of $C=gT/(2\pi)=$6.2–7.3 m/s and cover the horizontal distance between the stations ($\sim$100 km) in almost 4–5 h. As the recording interval is 3 h, a lagging of 2 time-intervals is exhibited. This is an important finding supporting the verification of SWAN model results and their proper association with in-situ data. On the contrary, cross-correlation results for the southward propagating waves reveal a lagging of 4 time-intervals (i.e., 12 h), indicating the relative influence of local winds, mostly from north, north-east and east directions (Fig. 4b).

3.3. SWAN results description and validation

The spatial distribution of significant wave heights and wave propagation direction over the Thracian Sea (coarse grid), for storm waves propagating from the south-east direction, is shown in Fig. 5a. The sheltering effect due to the presence of Thassos Island is evident and illustrated in the medium-scale grid (Fig. 5b). Finally, the wave field distribution at the nearshore area (fine resolution grid) depicts the significant wave energy reduction, due to the sheltering effect, along the Keramoti coastline (Fig. 5c). Indeed, significant wave heights appear diminished by 47%, as moving from Nestos River mouth (eastern coastline end) to Keramoti sand spit (central coastline part). At the same time,

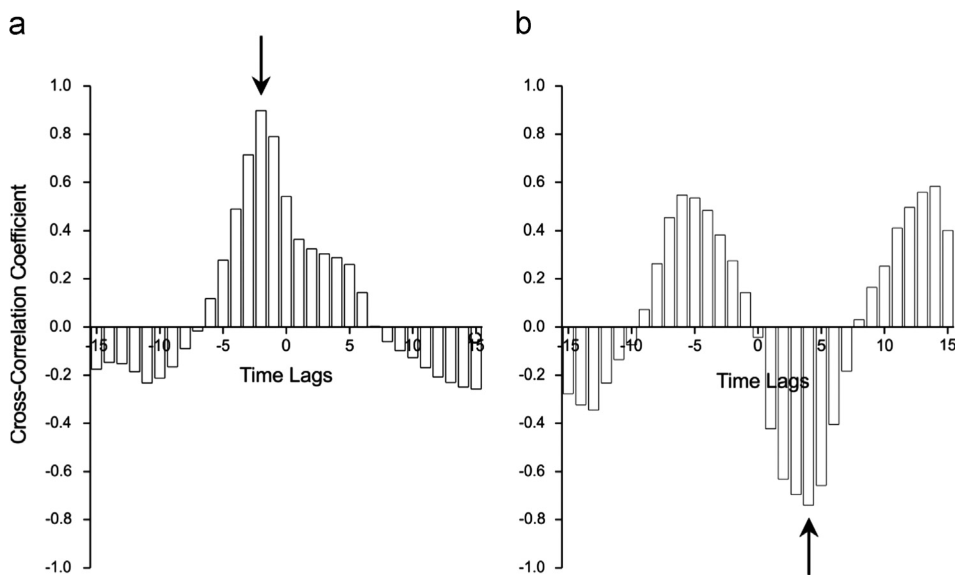

Fig. 4. Cross-correlation of significant wave height time-series measured at the nearshore and offshore sites, for: (a) waves entering the SWAN computational grid; and (b) waves exiting the SWAN computational grid.

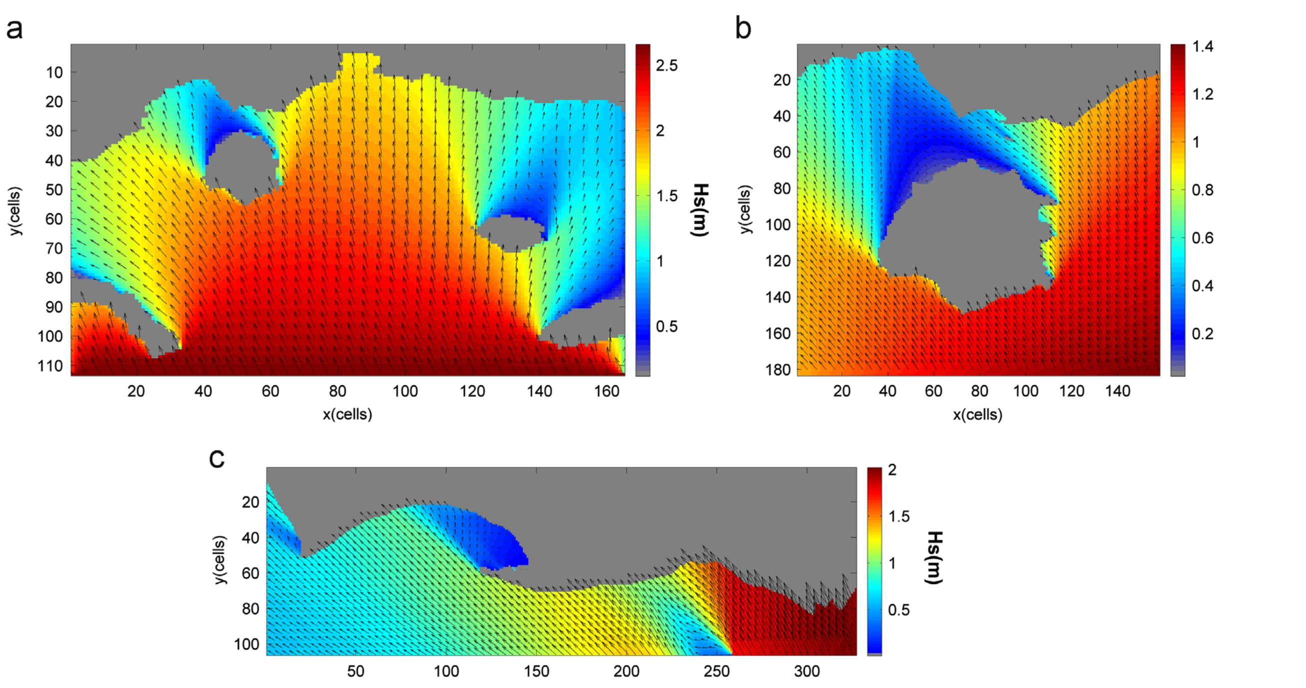

Fig. 5. Spatial distribution of significant wave height and wave direction, as computed by the triple-nesting SWAN model, in: (a) the coarse resolution grid; (b) the medium resolution grid; and (c) the nearshore fine resolution grid.

incident wave angles increase slowly from 111° at Nestos River mouth to 135° at Keramoti sand spit (measured anti-clockwisely from x-positive axis).

To compare model results to in-situ observations at the ADCP deployment site, model data were demarcated according to the wave conditions at the offshore station, into wave entering and wave exiting the computational grid conditions. Such demarcation arises from the different time-lags produced by the cross-correlation analysis of offshore and nearshore observed datasets. Model application in this area, appears to depict better results when the presence of large islands is treated as 'obstacles', especially when waves enter the computational grid at POSEIDON station (Fig. 6a). On the contrary, in cases that the waves exit the computational grid, propagating southwards under the influence north and north-east winds, better results are derived when islands are treated as 'land areas' (Fig. 6b).

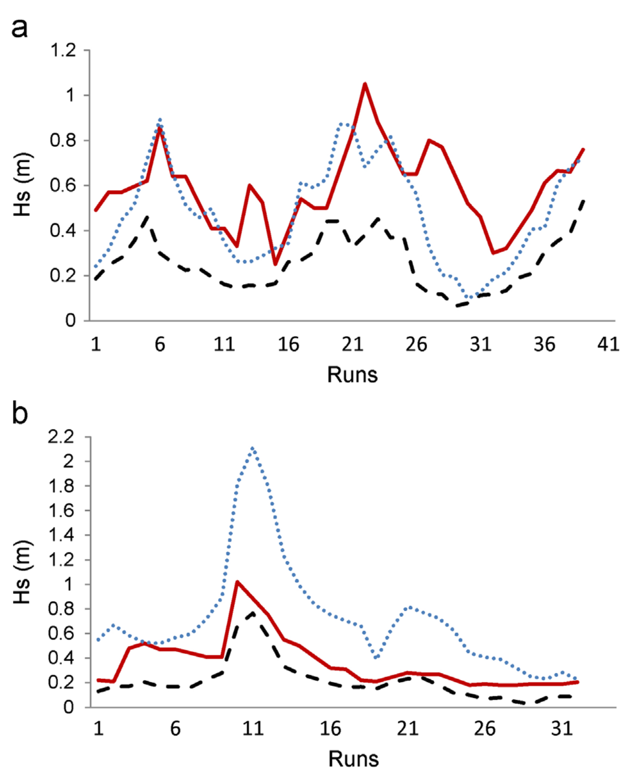

Fig. 6. Model results comparison to in-situ observed significant wave height at the ADCP deployment, for: (a) waves entering the SWAN computational grid; and (b) waves exiting the SWAN computational grid. Lines denote the observed H_S (solid line), the SWAN model results treating islands as 'land' (dotted line), and the SWAN model results treating islands as 'obstacles' (dashed line). (For interpretation of the references to color in this figure legend, the reader is referred to the web version of this article.)

Table 3
Statistical parameters to assess SWAN model performance.

	Incoming waves		Outgoing waves	
	H_S	T_P	H_S	T_P
R^2	0.82	0.62	0.57	0.09
RMSE	0.18	1.44	0.37	2.65
SI	0.25	0.30	0.24	0.34
Mean bias	−0.15	−0.50	−0.34	−1.99
IA	0.82	0.84	0.46	0.39
Mean absolute error (MAE)	0.15	1.03	0.16	2.00
Relative error (RE)	0.40	0.34	0.28	0.38

Table 3 illustrates the statistical parameters utilized to assess model performance in both cases. Model agreement with 2 time-lags reaches satisfactory levels, in significant wave height and wave period, as waves propagate northwards from North Aegean Sea to Thracian Sea. Under northern and north-east winds, the performance of SWAN tested for 4 time-lags appears significantly reduced, especially for wave period. The coupling of SWAN with ELCOM did not improve model performance on H_S and T_P. However, a significant improvement in the wave propagation direction was shown, as the mean direction error was reduced from 15.4° for the SWAN only case to 11.4° in the SWAN and ELCOM coupling case.

3.4. SWAN results for extreme winds and waves

Fig. 7 presents a semi-logarithmic plot of the wind empirical distribution function, the sample mean excess against thresholds, the Q–Q plot and the Hill tail index against different thresholds. A threshold determined at 12 m/s may be appropriate, as shown by these diagrams. A thin tailed distribution in the extreme wind values is shown by the convex departure from the straight line in the Q–Q plot. This finding suggests that $\xi<0$ and the tail is approximated by the Weibull distribution. Indeed, the shape of the mean excess curve (Fig. 8) indicates that the fitted model follows the Weibull model pattern, while the negative value of the shape parameter $\xi=-0.294$ with an error margin at 95% confidence interval at $[-0.41,-0.17]$. Our analysis exhibits that the other two GEV parameters have the following values: $\mu=13.478$, $\sigma=3.633$, and the corresponding 95% confidence intervals are [12.844, 14.112] and [3.17, 4.096], respectively. Since the fitted model belongs to the Weibull family, it is possible to make an inference on the upper end-point of the model, estimated as $z+=\mu-\sigma/\xi$ with a value of 26.005 m/s, having a 95% confidence interval [20.575; 38.206].

Similarly, the extreme value analysis for the significant wave heights at the POSEIDON buoy determined a threshold of $u_2=3.2$ m. A heavy-tailed distribution in the extreme wave values is obtained, as the shape parameter $\xi>0$. In fact $\xi=0.20$, with 95% confidence interval of [0.11, 0.29], implying that the distribution approaches slowly infinity (Fig. 8). Parameter estimation through the maximum likelihood method revealed that $\mu=1.86$ and $\sigma=0.75$ with an error margin at 95% confidence interval of [1.78, 1.99] and [0.69, 0.81], respectively.

Table 4 presents the results of POT analysis for wind speeds and significant wave heights at the offshore POSEIDON buoy for different return periods (25, 50 and 100 years). These results were imported as boundary conditions into the validated SWAN model to reproduce the response of the nearshore wave field under an extreme wind-wave event. An indicative result of the wave field at the three nested grids under the 50-year return period (wind speed of 27.11 m/s and significant wave height of 7.04 m) northward propagating wave event is shown in Fig. 9. Islands (Thassos and Samothraki) act as shelters for the propagating waves, reducing their height by 60% at their lee side (Fig. 9a). At the western part of the low resolution grid, the presence of Athos Peninsula diffracts the incident waves, reducing their energy as they propagate further northwards. This has a significant effect in the traveling of waves around Thassos Island (Fig. 9b), as waves with higher significant height are found at the island's eastern part ($H_S\sim6.8$ m), as compared to those propagating from the west ($H_S\sim6.0$ m). For this reason, at the sheltered part of the computational field, waves with diminished $H_S\sim3.1$ m tend to travel to the north-west direction, as eastern diffracted waves carry higher portions of energy than the western ones. At Keramoti coastline, these incident south-west waves exhibit variable significant wave height, ranging between 4.9 m at the western sheltered part

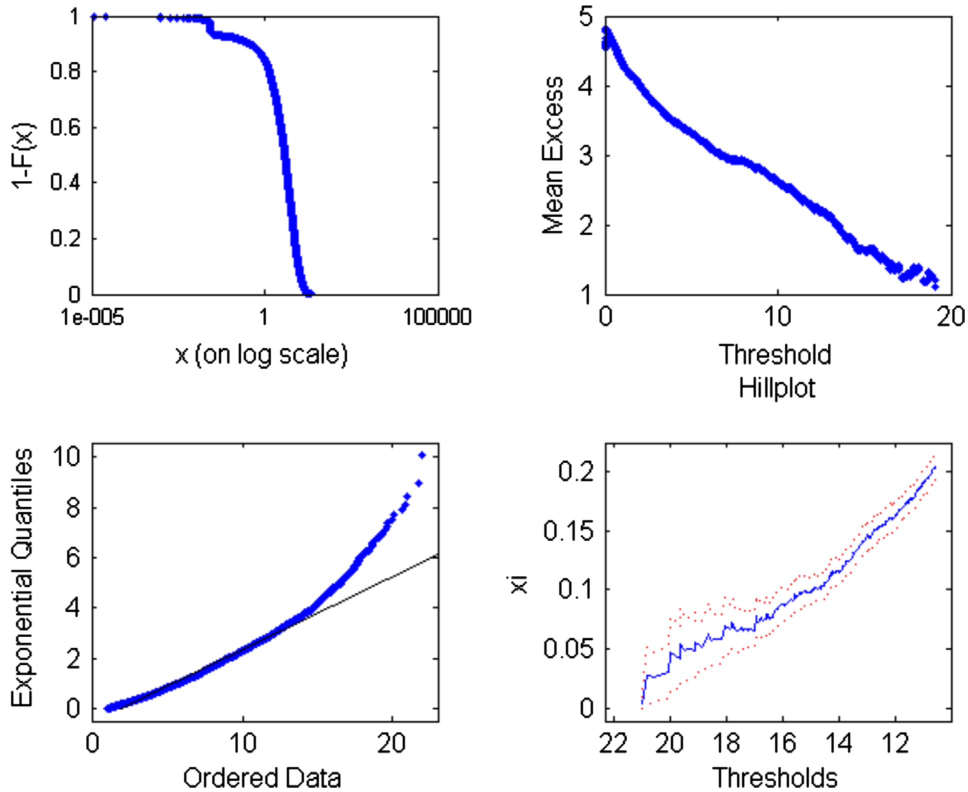

Fig. 7. Diagnostic plots for the GEV model applied on the wind POSEIDON dataset, where (a) the wind empirical distribution function, (b) the sample mean excess against thresholds, (c) the Q–Q plot and (d) the Hill tail index against different thresholds.

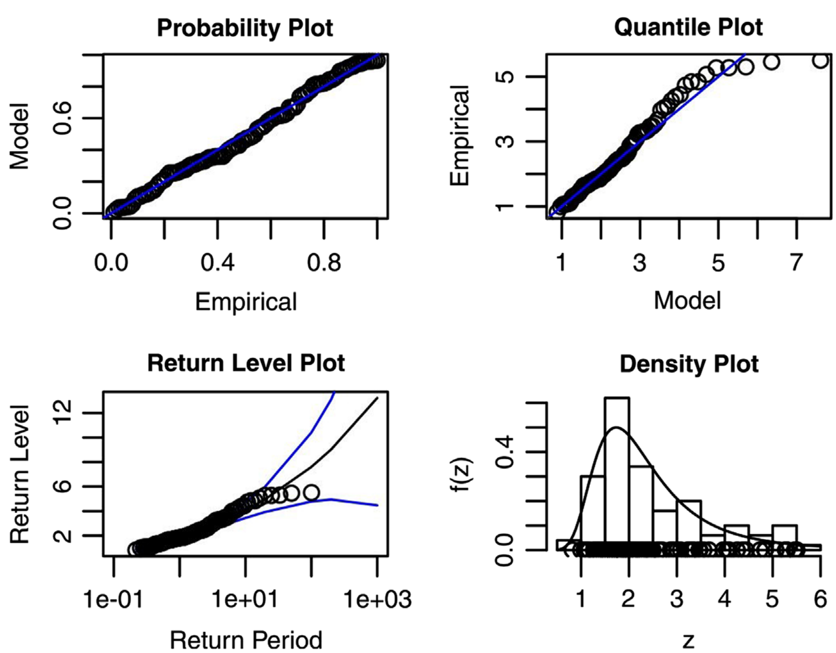

Fig. 8. Diagnostic plots for the GEV model applied on the wave POSEIDON dataset, where (a) the probability plot, (b) the quantile plot, (c) the return level plot and (d) density function plot.

Table 4
Return values for 25, 50 and 100 years produced by the GEV with 95% confidence intervals.

	25-year	50-year	100-year
Wind speed (m/s)	25.39 (23.95, 26.10)	27.11 (25.93, 28.36)	28.37 (27.42, 30.06)
Significant wave height (m)	5.39 (4.15, 6.13)	7.04 (5.23, 8.25)	6.83 (5.82, 9.71)

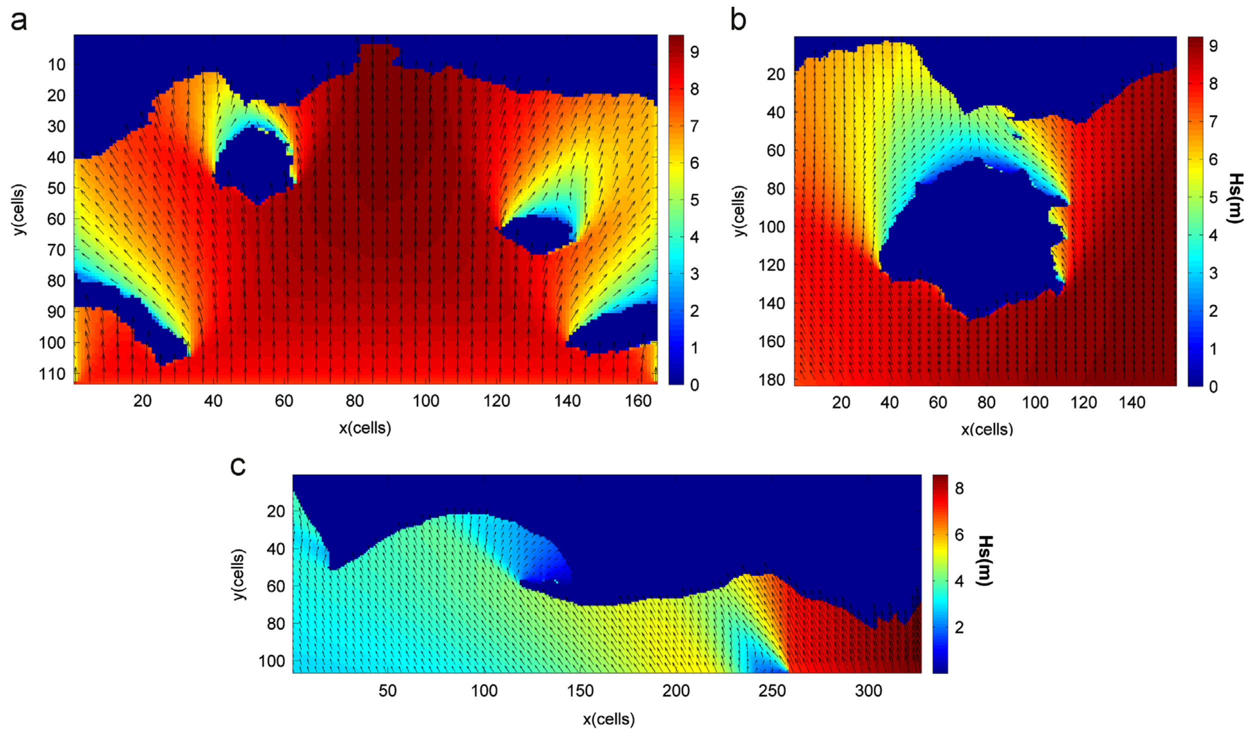

Fig. 9. Spatial distribution of significant wave height and wave direction, during an extreme wind and wave event with 50 years return period, as computed by the triple-nesting SWAN model, in: (a) the coarse resolution grid; (b) the medium resolution grid; and (c) the nearshore fine resolution grid.

to 6.8 m at the eastern exposed part of the shoreline (Fig. 9c). Wave angles range between 88° and 113°, respectively (measured anti-clockwisely from *x*-positive axis). Most of the wave energy appears concentrated at 0.85 Hz at the western part until 0.51 Hz at the exposed eastern shoreline.

4. Discussion

In-situ wave data analysis and SWAN model results revealed that the wave field along the sheltered by Thassos Island coastline appears influenced by the offshore winds and the consequent waves propagation. However, local wave growth in the nearshore zone is also evident. Higher wave heights and periods originate from the east and south-east directions, corresponding to the longer fetches (~160 km). SWAN stationary-mode model application in the study area appears to exhibit better results under the configuration of islands and peninsulas as obstacles of zero transmissivity and reflectivity, especially for southern waves entering the low resolution computational grid. Such configuration implies that the sides of the island are not sloping under the sea surface, thus avoiding wave refraction. Similar improvement in model efficiency in the nearshore zone was also seen when treating islands as 'land', in the cases when waves exit the low-resolution computational grid influenced by north and north-eastern winds.

SWAN results underestimations of significant wave height may be attributed to the link of the overall modeled diffraction effect on spatial resolution of the nearshore computational grid, as shown by Rusu et al. (2008). At the same time, the triad nonlinear interactions may also become significant at the nearshore zone, intensifying the transfer of wave energy across the wave spectrum, thus underestimating the actually observed conditions. Rusu et al. (2008) improved their validation results when after nearshore nesting, SWAN was switched from spherical to Cartesian coordinates, and diffraction and triad nonlinear interactions were activated.

The ability of SWAN performing under the stationary mode to reproduce the transformation of wave energy in shallow areas has been reported by several authors (Kaiser and Niemeyer, 1999; Niemeyer and Kaiser, 2001; Browne et al., 2007; Gorrel et al., 2011). The stationary model appears inaccurate as it responds too quickly to the wave shift, creating new energy and destroying the old (Rogers et al., 2007). Further, model stationarity requires the time of propagation of the waves through the domain to be short compared to the variation of water level, currents and changes in offshore wave conditions (Browne et al., 2007). Cross-correlation analysis between offshore and nearshore wave-series revealed a time-lag of 6 h for northwards propagating waves and 12 h for south propagating waves, indicating that a non-stationary approach could be more appropriate. However, in the non-stationary mode the time-step should be small enough such that a wave energy packet does not travel a distance of more than one grid cell during any given time step (Rogers et al., 2007). In the unconditionally stable non-stationary SWAN scheme this requirement is removed, but accuracy of the scheme falls off considerably when the wave energy travels much more than 2–4 grid cells per time step (Rogers et al., 2002). As the nearshore grid has a horizontal spacing of only 50 m, such requirement increases considerably the computational time of the model.

Herman et al. (2009) explained that the significant underestimations of wave height and peak period observed by SWAN could be attributed to the usage of non-consistent spectral frequency ranges when calculating the mean wave parameters during model verification, especially at shallow, sheltered locations. This explains well the moderate SWAN performance in wave periods (Table 3), as SWAN tends to underestimate the low frequency energy part and to over-estimate the higher frequency energy spectrum. Rusu et al. (2008) also reports limited SWAN model efficiency in peak periods and rather better in mean periods in sheltered by islands areas of Madeira Archipelago. SWAN results are expected to be more reliable at the eastern part of Thassos Passage in terms of significant wave height and peak wave period. Concerning wave direction, since the numerical model described satisfactorily the wave transformation due to diffraction and bathymetry change at the more complex western part of the channel, reliable results are also expected at its eastern part.

SWAN ability to effectively assess wave propagation direction in the studied area was rather poor, but significant improvement was shown when the spectral wave model was coupled to the hydrodynamic. The hydrodynamic model ELCOM was coupled to SWAN at the high resolution nearshore grid, providing the velocity field and receiving the radiation stresses field in each time-step. Similar, low model-to-measurement differences have been reported by Dietrich et al. (2011), using the coupled SWAN and ADCIRC model. Wolf and Prandle (1999) named this effect as 'current diffraction', as the higher frequency waves tend to turn towards the direction of the currents. The presence of Thassos Island in a short distance to Keramoti coastline forms Thassos Passage, a narrow channel enhancing alongshore flow and encouraging vertical mixing. Strong tidal currents (up to 1.5 m/s) develop in this channel, affecting directly the wave propagation in the nearshore zone (Sylaios et al., 2013). Indeed, under a westward flow field in Thassos Passage, modeled waves tend to turn towards north-west direction, in better agreement with ADCP data. This effect is more evident during low period waves (4–6 s), in agreement to theoretical considerations. On the contrary, under eastern currents, modeled waves appear slightly twisted to the west, increasing the error by $\sim 10^{\circ}$ with the observed wave results.

To estimate the extremes of the wave height distribution the POT method was applied to reveal the wind speeds and wave heights at the offshore boundary having return periods of 25, 50 and 100 years. Model results indicate that although a wave of 7.0 m propagates at the offshore North Aegean Sea, at the sheltered by Thassos Island nearshore zone a 60% reduction in wave energy exists. Waves reaching the coastline from the south-west direction exhibit diffraction at Athos Peninsula, leading to a decrease in wave heights field, although not very important, since diffraction in SWAN is sensitive to grid resolution and this peninsula is modeled by the low resolution grid. At the medium resolution grid, as waves approach from south-west and south-east directions, due to the presence of Thassos Island, important along-channel wave height gradients are induced, as south-east waves are more energetic at the nearshore zone. South-east waves affect the transfer and distribution of sediments along the Keramoti coastline, favoring coastal erosion at the eastern part of the passage and inducing a net westward littoral transport (Sylaios et al., 2012). River suspended matter and coastal eroded material is accreted at an along-channel sandbar at the western part of Keramoti coastline (Sylaios et al., 2013).

Continuation of this work will include running SWAN in a forecast mode, in association to predicted offshore wave boundary conditions, using a validated fuzzy logic model (Sylaios et al., 2009). Detailed forecasts of wave conditions at the nearshore zone are required in regions where extensive sediment transport phenomena take place. The cost of running such model could be moderate, with 9 h forecasts completed in less than 1 h.

5. Conclusions

The application of a coupled SWAN and ELCOM model was presented, nested at three grids of gradually increased spatial resolution, aiming to simulate the nearshore wave field at the lee of Thassos Island (North Aegean Sea). The stationary model mode was used, with wind and waves boundary conditions provided by the offshore POSEIDON buoy. Model results were validated against in-situ observations utilizing the directional wave data from an ADCP deployment. Data comparison revealed that SWAN represented quite well the significant wave heights along the Keramoti shoreline, for both entering and exiting the broad-scale computational grid waves. Underestimations are evident in SWAN results of significant wave height and peak period, especially for waves entering the low-resolution computational grid. Current diffraction was the main mechanism to correct wave propagation directions at the nearshore zone, especially under the more prominent western circulation.

The validated model was run under various extreme wind and wave incidents with return periods of 25, 50 and 100 years. A 60% reduction in the incident wave height is achieved due to the sheltering effect produced by Thassos Island. South-eastern waves transfer higher wave energy at the nearshore, as the south-western branch is diffracted at Athos Peninsula.

Acknowledgments

This research has been co-financed by the European Union (European Social Fund – ESF) and Greek national funds through the Operational Program "Education and Lifelong Learning" of the National Strategic Reference Framework (NSRF) - Research Funding Program: Heracleitus II. Investing in knowledge society through the European Social Fund.

References

Alari, V., Raudsepp, U., Kõuts, T., 2008. Wind wave measurements and modelling in Küdema Bay, Estonian Archipelago Sea. Journal of Marine Systems 74, S30–S40.
Booij, N., Ris, R.C., Holthuijsen, L.H., 1999. A third-generation wave model for coastal regions. 1. Model description and validation. Journal of Geophysical Research C104, 7649–7666.
Breivik, Ø., Gusdal, Y., Furevik, B.R., Aarnes, O.J., Reistad, M., 2009. Nearshore wave forecasting and hindcasting by dynamical and statistical downscaling. Journal of Marine Systems 78, S235–S243.
Browne, M., Castelle, B., Strauss, D., Tomlinson, R., Blumenstein, M., Lane, C., 2007. Near-shore swell estimation from a global wind-wave model: spectral process, linear, and artificial neural network models. Coastal Engineering 54, 445–460.
Caliskan, H., Valle-Levinson, A., 2008. Wind-wave transformations in an elongated bay. Continental Shelf Research 28, 1702–1710.
Cassulli, V., Cheng, R.T., 1992. Semi-implicit finite difference methods for three-dimensional shallow water flow. International Journal for Numerical Methods in Fluids 25, 629–648.
Cavaleri, L., Malanotte-Rizzoli, P., 1981. Wind wave prediction in shallow water theory and applications. Journal of Geophysical Research 86, 10961–10973.
Coles, S.G., 2001. An introduction to statistical modelling of extreme value. Springer, London.
Cuchiara, D.C., Fernandes, E.H., Strauch, J.C., Winterwerp, J.C., Calliari, L.J., 2009. Determination of the wave climate for the southern Brazilian shelf. Continental Shelf Research 29, 545–555.
Dietrich, J.C., Zijlema, M., Westerink, J.J., Holthuijsen, L.H., Dawson, C., Luettich Jr., R.A., Jensen, R.E., Smith, J.M., Stelling, G.S., Stone, G.W., 2011. Modeling hurricane waves and storm surge using integrally-coupled, scalable computations. Coastal Engineering 58, 45–65.
Dietrich, J.C., Tanaka, S., Westerink, J.J., Dawson, C.N., Luettich Jr., R.A., Zijlema, M., Holthuijsen, L.H., Smith, J.M., Westerink, L.G., Westerink, H.J., 2012. Performance of the unstructured-mesh, SWAN+ADCIRC model in computing hurricane waves and surge. Journal of Scientific Computing 52 (2), 468–497.
Dragani, W.C., Martin, P.B., Simionato, C.G., Campos, M.I., 2010. Are wind wave heights increasing in south-eastern south American continental shelf between 32°S and 40°S? Continental Shelf Research 30, 481–490.
Dykes, J.D., Wang, D.W., Book, J.W., 2009. An evaluation of a high-resolution operational wave forecasting system in the Adriatic Sea. Journal of Marine Systems 78, S255–S271.
Gençay, R., Selçuk, F., Ulugülyağci, A., 2001. EVIM: a software package for extreme value analysis in MATLAB. Studies in Nonlinear Dynamics and Econometrics 5, 213–239.
Gorrel, L., Raubenheimer, B., Elgar, S., Guza, R.T., 2011. SWAN predictions of waves observed in shallow water onshore of complex bathymetry. Coastal Engineering 58, 510–516.
Herman, A., Kaiser, R., Niemeyer, H.D., 2009. Wind-wave variability in a shallow tidal sea—spectral modelling combined with neural network methods. Coastal Engineering 56, 759–772.

Hodges, B.R., Imberger, J., Saggio, A., Winters, K.B., 2000. Modelling basin scale internal waves in a stratified lake. Limnology and Oceanography 45 (7), 1603–1620.
Hodges, B., Dallimore, C., 2001. Estuary and Lake Computer Model: ELCOM Science Manual Code Version 2.0.0. Centre for Water Research, University of Western Australia, Perth.
Kaiser, R., Niemeyer, H.-D., 1999. Changing of local wave climate due to ebb-delta migration. In: Proceedings of the 26th International Conference on Coastal Engineering. ASCE, Copenhagen, Denmark.
Kamidis, N., Kamidis, N., Sylaios, G., Tsihrintzis, V.A., 2011. Modeling the Nestos River plume dynamics using ELCOM. Desalination and Water Treatment 33, 22–35.
Kokkos, N., Sylaios, G., 2012. Simulation of the three-dimensional hydrodynamic circulation in North Aegean Sea using ELCOM model. In: Proceedings of the 10th Panhellenic Symposium of Oceanography and Fisheries, Athens, 7–11/5/2012.
Komen, G.J., Cavaleri, L., Donelan, M., Hasselmann, K., Hasselmann, S., Janssen, P.A.E.M., 1994. Dynamics and Modelling of Ocean Waves. Cambridge University Press, Cambridge, UK.
Lee, B-C., Chien, H., Cheng, H-Y., Chiou, M-D., 2010. Evaluation of operational wave forecasts for the Northeastern coast of Taiwan. Terrestrial, Atmospheric and Oceanic Sciences 21, 195–210.
Liu, H-W., Pengzhi, L., Jothi Shankar, N., 2004. An analytical solution of the mild-slope equation for waves around a circular island on a paraboloidal shoal. Coastal Engineering 51, 421–437.
Niclasen, B.A., Simonsen, K., 2005. Current Induced Variations in Measured Wave Parameters in Data from the Faroe Islands. Technical Report. Faculty of Science and Technology, Faroe Islands, 46 pp.
Niemeyer, H.-D., Kaiser, R., 2001. Design wave evaluation for coastal protection structures in the Wadden Sea. In: Proceedings of the International Conference on Ocean Wave Measurement and Analysis, Reston, VA, USA.
Rogers, W.E., Kaihatu, J.M., Petit, H.A.H., Booij, N., Holthuijsen, L.H., 2002. Diffusion reduction in an arbitrary scale third generation wind wave model. Ocean Engineering 29, 1357–1390.
Rogers, W.E., Kaihatu, J.M., Hsu, L., Jensen, R.E., Dykes, J.D., Holland, K.T., 2007. Forecasting and hindcasting waves with the SWAN model in the Southern California Bight. Ocean Engineering 54, 1–15.
Rusu, E., Pilar, P., Guedes Soares, C., 2008. Evaluation of the wave conditions in Madeira Archipelago with spectral models. Ocean Engineering 35, 1357–1371.
Simiu, E., Heckert, N., 1996. Extreme wind distribution tails: a peaks over threshold approach. Journal of Structural Engineering 122 (5), 539–547.
Soukissian, T.H., Chronis, G.Th., Nittis, K., 1999. POSEIDON: operational marine monitoring system for Greek seas. Sea Technology 40 (7), 32–37.
Soukissian, T.H., Prospathopoulos, A.M., Diamanti, C., 2002. Wind and wave data analysis for the Aegean Sea – preliminary results. The Global Atmosphere and Ocean System 8, 163–189.
Sylaios, G., Bouchette, F., Tsihrintzis, V.A., Denamiel, C., 2009. A fuzzy inference system for wind-wave modeling. Ocean Engineering 36, 1358–1365.
Sylaios, G., Anastasiou, S., Tsihrintzis, V.A., 2012. Restoration of a seashore eroded due to dam operation through beach nourishment. Ecohydrology and Hydrobiology 12 (2), 123–135.
Sylaios, G., Kamidis, N., Anastasiou, S., Tsihrintzis, V.A., 2013. Hydrodynamic response of Thassos Passage (N. Aegean Sea) to Nestos River discharge and meteorological forcing. Continental Shelf Research 59, 37–51.
Willmott, C.J., Ackleson, S.G., Davis, R.E., Feddema, J.J., Klink, K.M., Legates, D.R., O'Donnell, J., Rowe, C.M., 1985. Statistics for the evaluation of model performance. Journal of Geophysical Research 90 (C5), 8995–9005.
Wolf, J., Prandle, D., 1999. Some observations of wave–current interaction. Coastal Engineering 37, 471–485.